Supplement to "Processes limiting the emergence of detectable aerosol indirect effects on tropical warm clouds in global aerosol-climate model and satellite data"

by

Karsten Peters, Johannes Quaas, Philip Stier and Hartmut Graßl

May 10, 2014

1 Effects of alternative placements of the mid Atlantic main shipping lane

We state that the locations of the main shipping lanes used to indicate the "track" position in the plots of Figs. 1 and 2 of the main paper were chosen as to represent the windward edge of the main shipping corridor. Especially in the mid Atlantic ocean, this approach renders the maximum in shipping emissions slightly inside the "polluted" part of the corridor, i.e. the maximum is not located directly at the position of the imposed shipping lane.

This may cause some confusion as to whether we are actually in the position of adequately separating clean from polluted conditions, especially in the mid Atlantic Ocean region where the maximum in shipping emissions occurs about 3° off the position of the imposed shipping lane. Here, we show the effect of longitudinally displacing the originally used position of the shipping lane towards the maximum of emissions in the mid Atlantic Ocean. Fig. S1 shows the spatial distribution of sulfuric-species emissions from ships as used in simulation **Bsc** [Peters et al., 2012] overlain by with the originally used [Peters et al., 2011] and two alternative positions of the main shipping lane ("track"). Fig. S2 is similar to Fig. 1 in the main paper and shows the across corridor gradients of sulfuric emissions from ships for the three cases.

From Fig. S1 it is apparent that the width of the shipping emission maximum in the mid Atlantic Ocean makes it difficult to exactly define a distinct shipping lane – the emissions are rather spread out over the whole corridor. Thus, achieving placement of the main "track" at the maximum of emissions requires a 3° westward shift compared to the originally used definition (cf. Fig. S2). However, this procedure does not allow for a clear distinction between clean and polluted regions because the entire shipping corridor (from -5° to +5°) is subject to non-negligible shipping emissions.

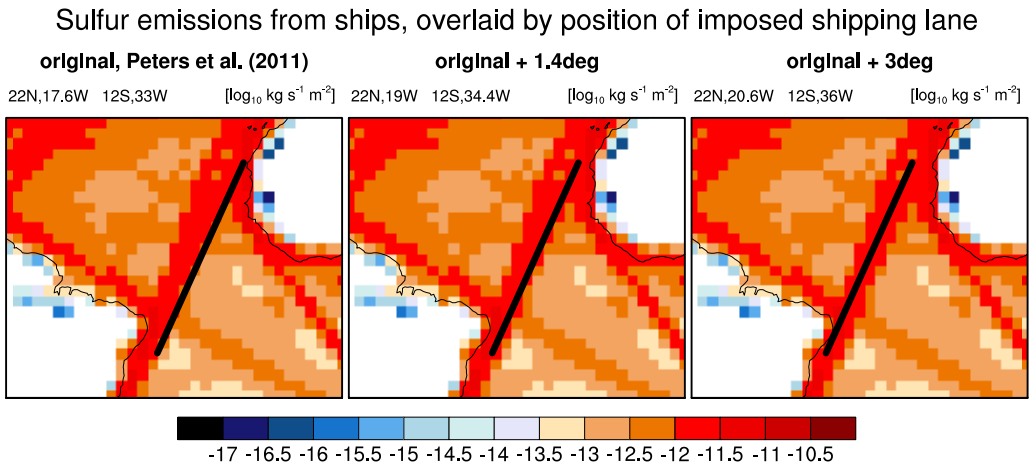

Figure S1: Sulfuric emissions from ships as used in simulation **Bsc** [Peters et al., 2012] with different positions of the imposed main shipping land overlaid. Left: track position as used in Peters et al. [2011] ("original"), middle: original track position shifted 1.4° westward, right: original track position shifted 3° westward.

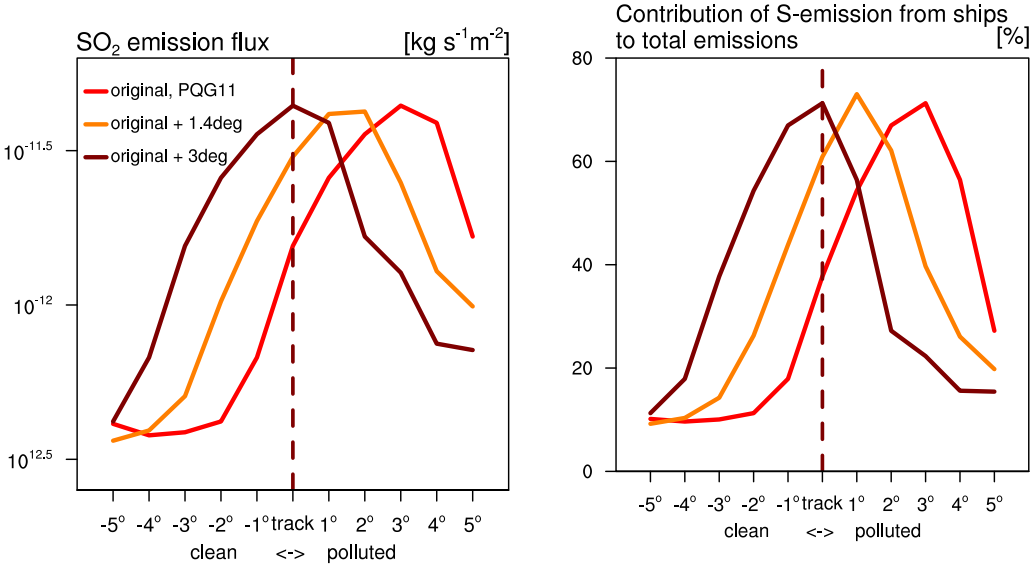

Figure S2: Across-corridor shipping emission profiles as implemented in simulation **Bsc** [Peters et al., 2012] for the mid Atlantic Ocean using the three imposed main shipping lane positions shown in Fig. S1. **Left panel:** Annual mean ship-emission fluxes ($\log_{10}$ scale); **right panel:** Share of the sulphur (S) emissions from ships in the total simulated S emission fluxes in [%] derived from $\left(\frac{\mathrm{S_{ship}(\mathbf{Bsc})}}{\mathrm{S_{total}(\mathbf{Bsc})}} \cdot 100\right)$. Shipping emissions are averaged to the T63 model resolution prior to calculating across-corridor profiles.

Therefore, we stick to the originally proposed location of the mid Atlantic shipping lane [Peters et al., 2011] which in our view adequately marks the distinct across-corridor increase in shipping emissions compared to the atmospheric background. The same holds for the other two shipping corridors, albeit the offset of the emission maximum is not as much displaced from the "track" as in the mid Atlantic Ocean.

2 Across corridor aerosol and cloud properties for the mid Indian Ocean and SE Pacific Ocean shipping corridors

See Figures S3 and S4.

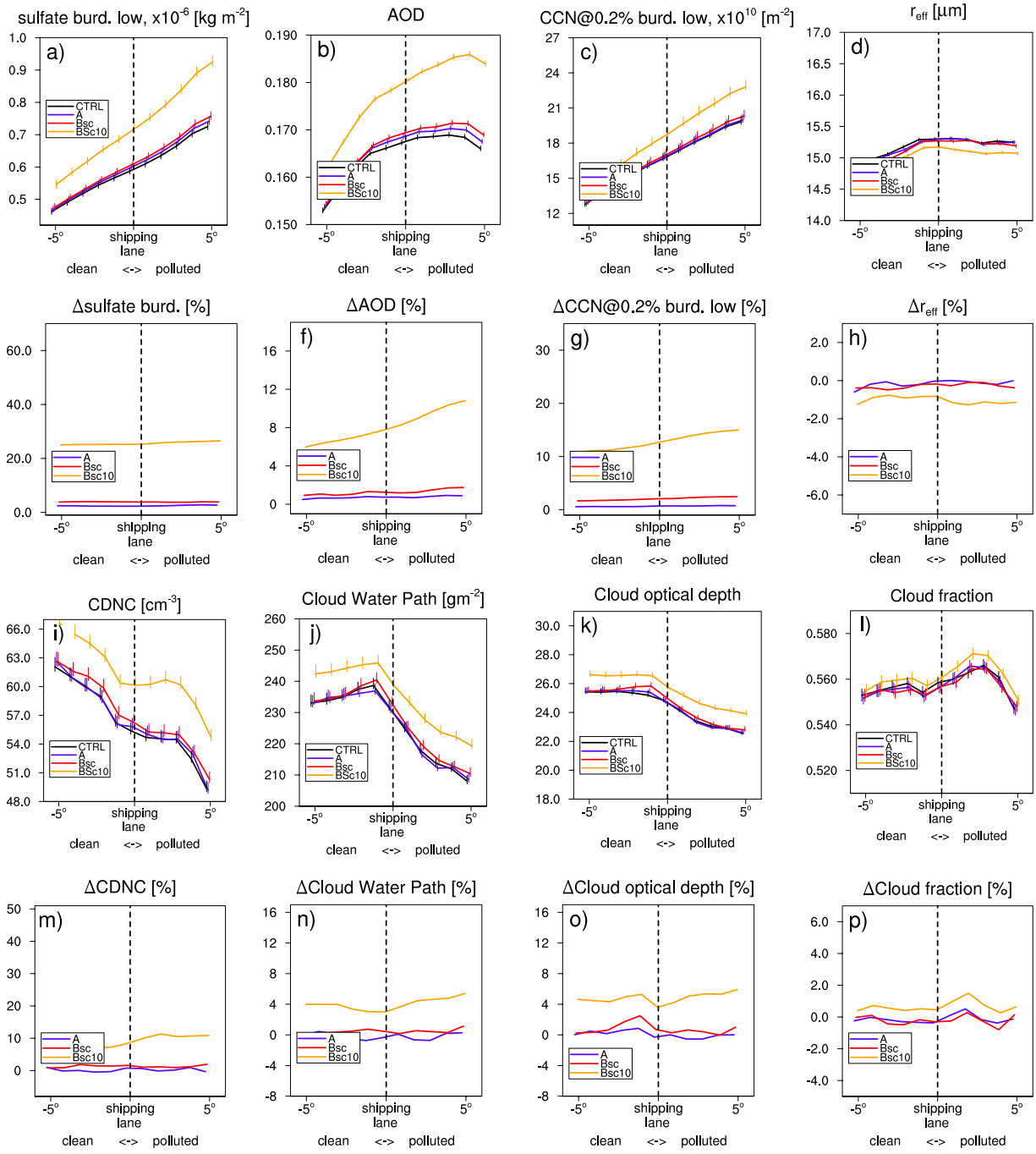

Figure S3: Across-corridor profiles of selected model diagnostics for the SE Pacific Ocean shipping corridor, absolute and relative values are shown: sulfate burden integrated over the lower troposphere (a, e), AOD (b, f), CCN(0.2%) burden integrated over the lower troposphere (c, g), cloud droplet effective radius r_{eff} at cloud top (d, h), cloud droplet number concentration CDNC at cloud top (i, m), cloud water path (j, n), cloud optical depth (k, o) and cloud fraction (maximum overlap assumed) (l, p). The error bars denote the confidence in the calculated mean value toward higher/lower values as given by $e_l = \sum_{i=0}^{N_l} \sqrt{(\bar{x} - l_i)^2} \left(\sqrt{N_l}\right)^{-1}$ and $e_u = \sum_{i=0}^{N_u} \sqrt{(\bar{x} - u_i)^2} \left(\sqrt{N_u}\right)^{-1}$, where e_l and e_u are the lower and upper bounds, $\bar{x}$ the mean value, l_i and u_i the samples smaller and larger than the mean and N_l and N_u the number of samples smaller and large than the mean, respectively. Relative changes are derived after $\left(\frac{\text{“simulation”} - CTRL}{CTRL} \cdot 100\right)$.

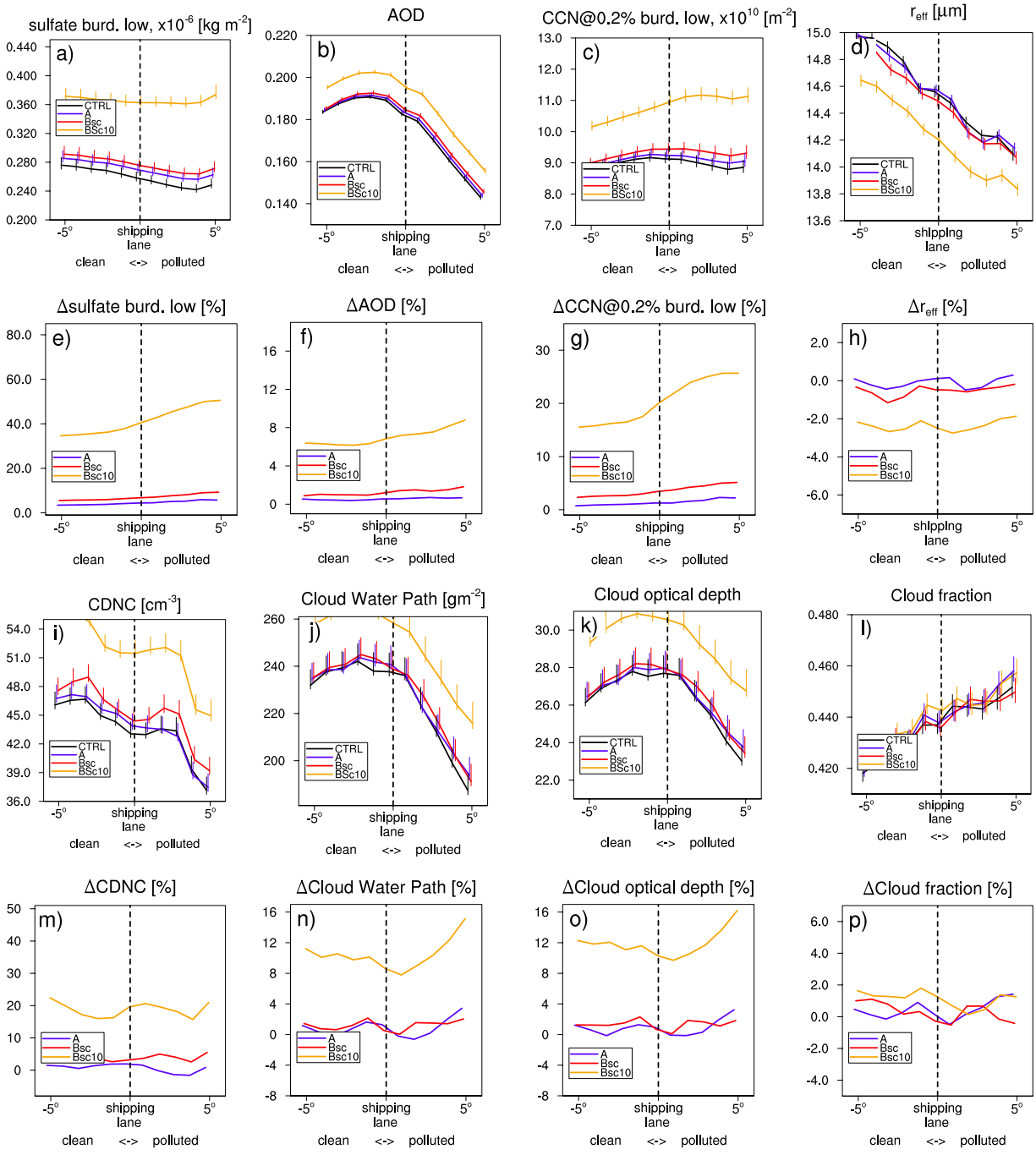

Figure S4: As Fig. S3, but for the mid Indian Ocean shipping corridor.

3 Season-wise composites of across corridor aerosol and cloud properties

See Figures S5 – S8.

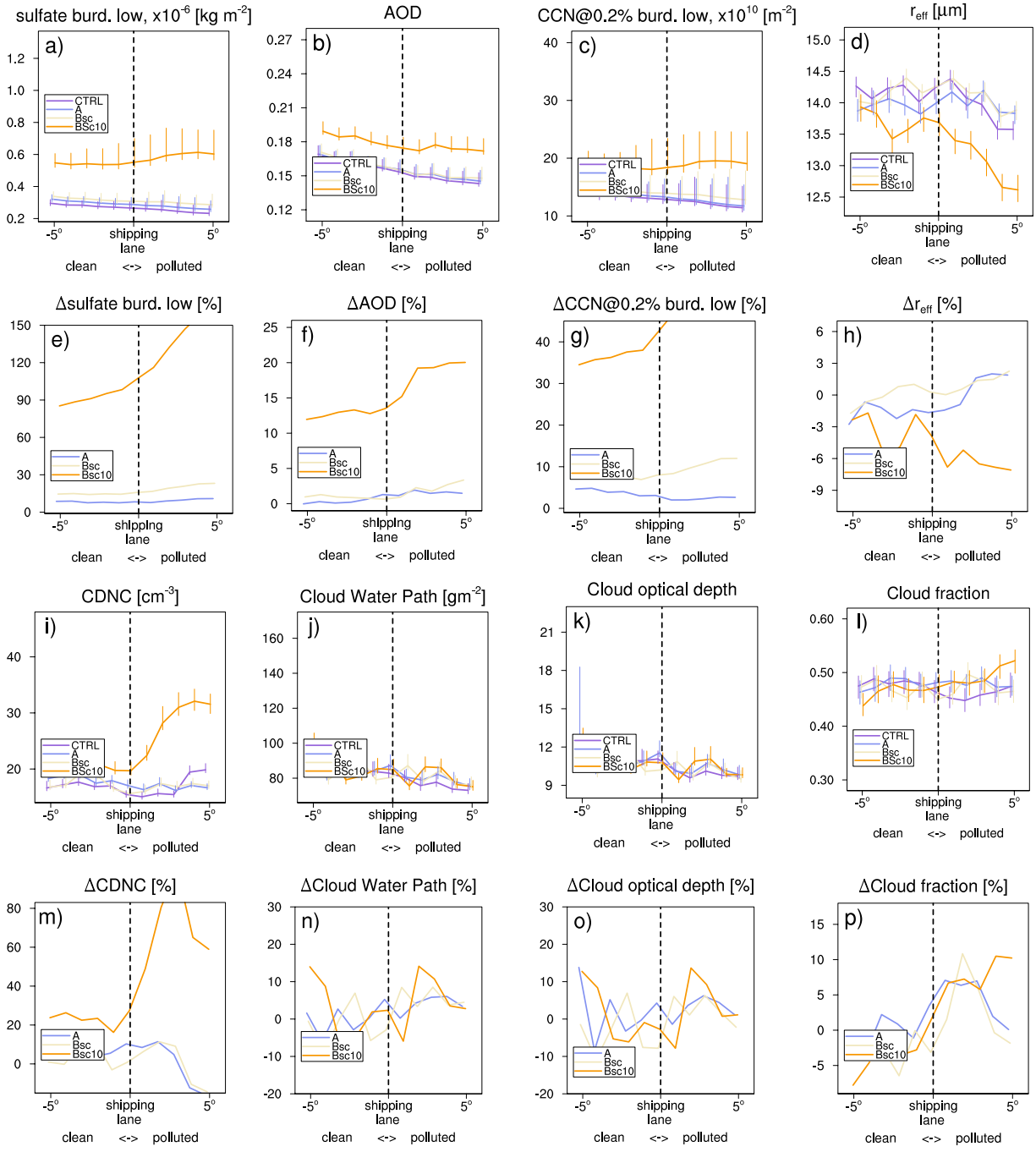

Figure S5: Across-corridor profiles of selected model diagnostics for the mid Atlantic shipping corridor, absolute and relative values are shown for season MAM: sulfate burden integrated over the lower troposphere (a, e), AOD (b, f), CCN(0.2%) burden integrated over the lower troposphere (c, g), cloud droplet effective radius r_{eff} at cloud top (d, h), cloud droplet number concentration CDNC at cloud top (i, m), cloud liquid water path (j, n), cloud optical depth (k, o) and cloud fraction (maximum overlap assumed) (l, p). The error bars denote the confidence in the calculated mean value toward higher/lower values as given by $e_l = \sum_{i=0}^{N_l} \sqrt{(\bar{x} - l_i)^2} \left(\sqrt{N_l}\right)^{-1}$ and $e_u = \sum_{i=0}^{N_u} \sqrt{(\bar{x} - u_i)^2} \left(\sqrt{N_u}\right)^{-1}$, where e_l and e_u are the lower and upper bounds, $\bar{x}$ the mean value, l_i and u_i the samples smaller and larger than the mean and N_l and N_u the number of samples smaller and large than the mean, respectively. Relative changes are derived after $\left(\frac{\text{“simulation”} - CTRL}{CTRL} \cdot 100\right)$.

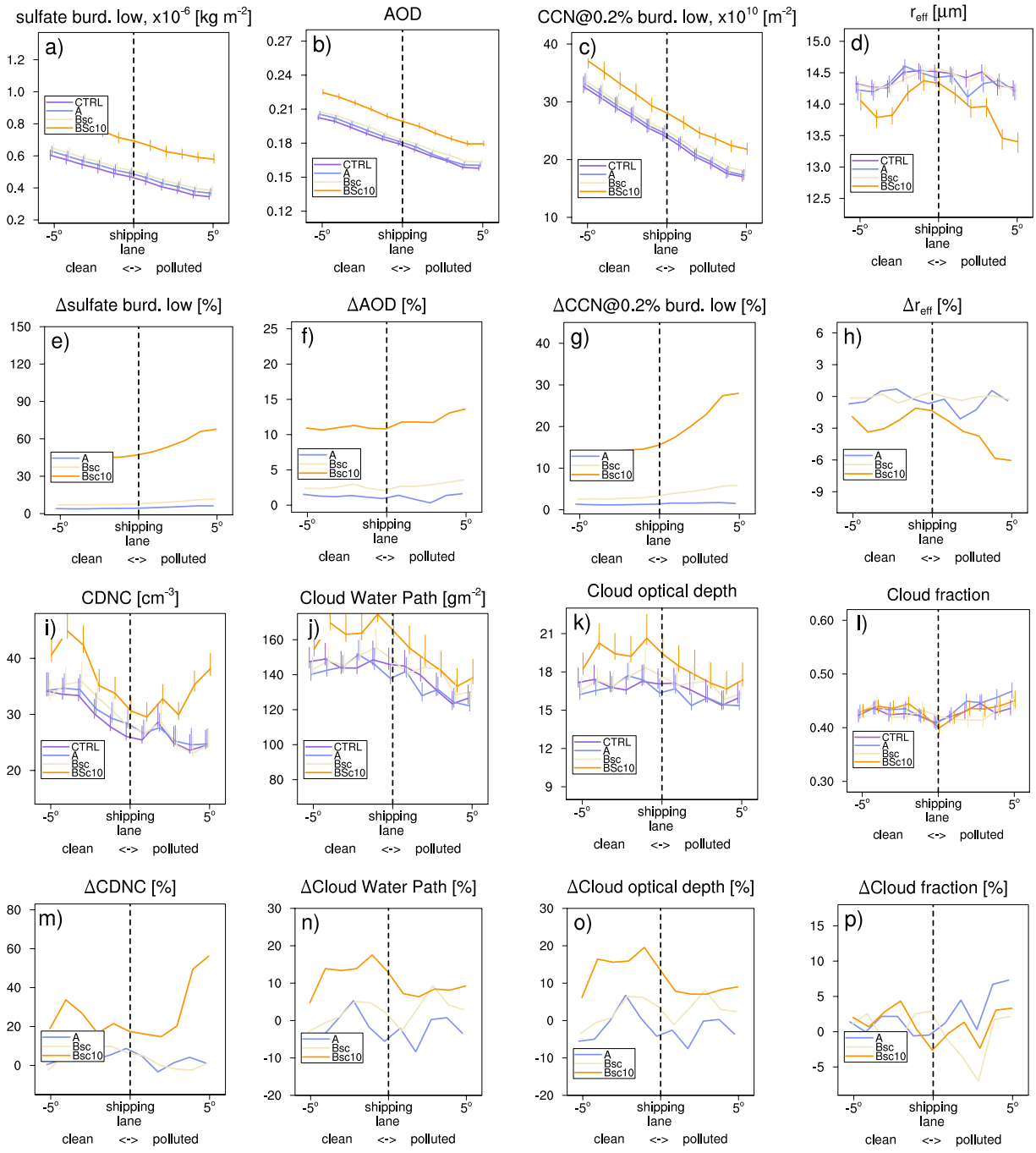

Figure S6: See Fig. S5, for season JJA

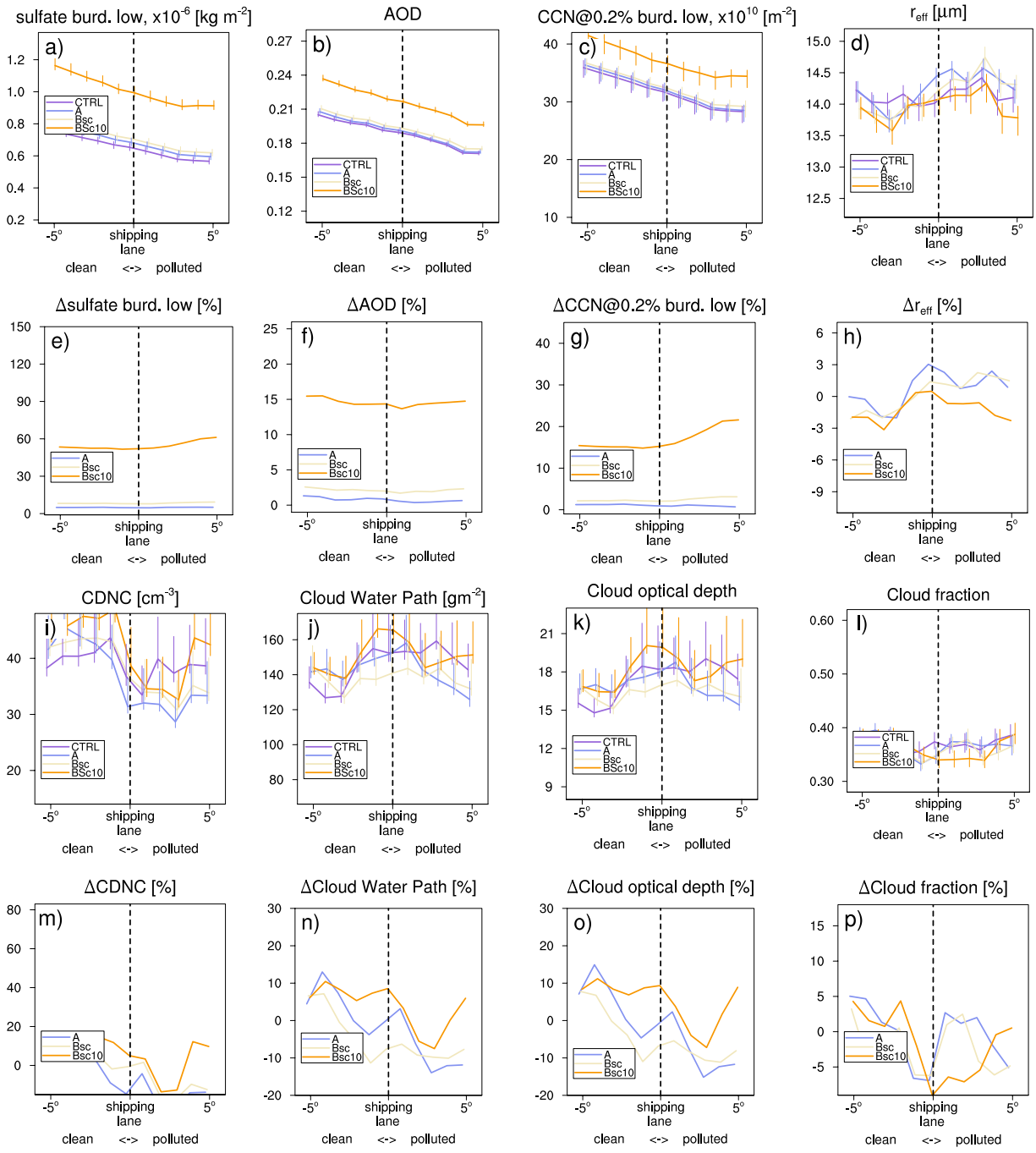

Figure S7: See Fig. S5, for season SON

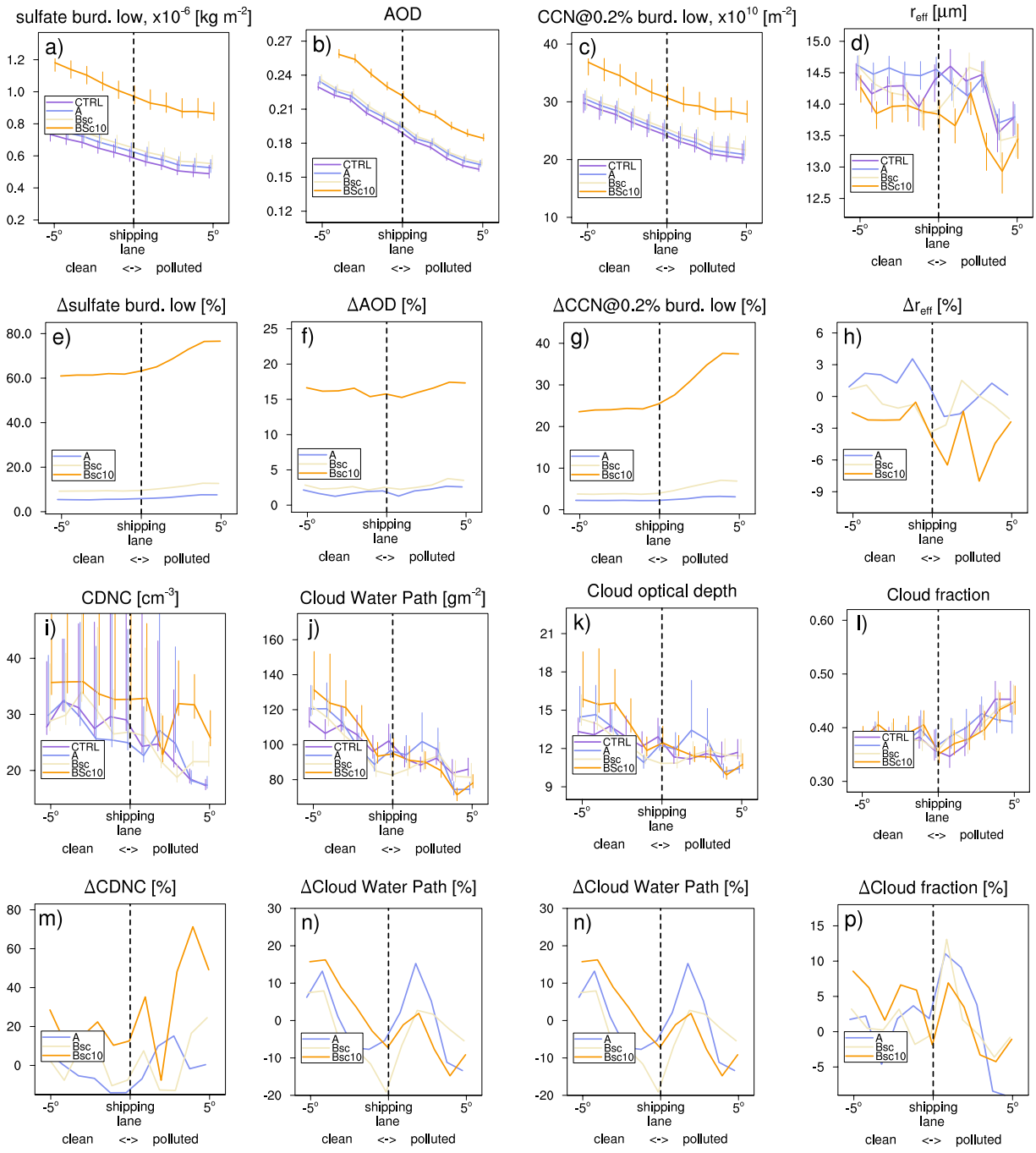

Figure S8: See Fig. S5, for season DJF

4 Season-wise composites of spatially distributed model diagnostics

See Figures S9 – S12.

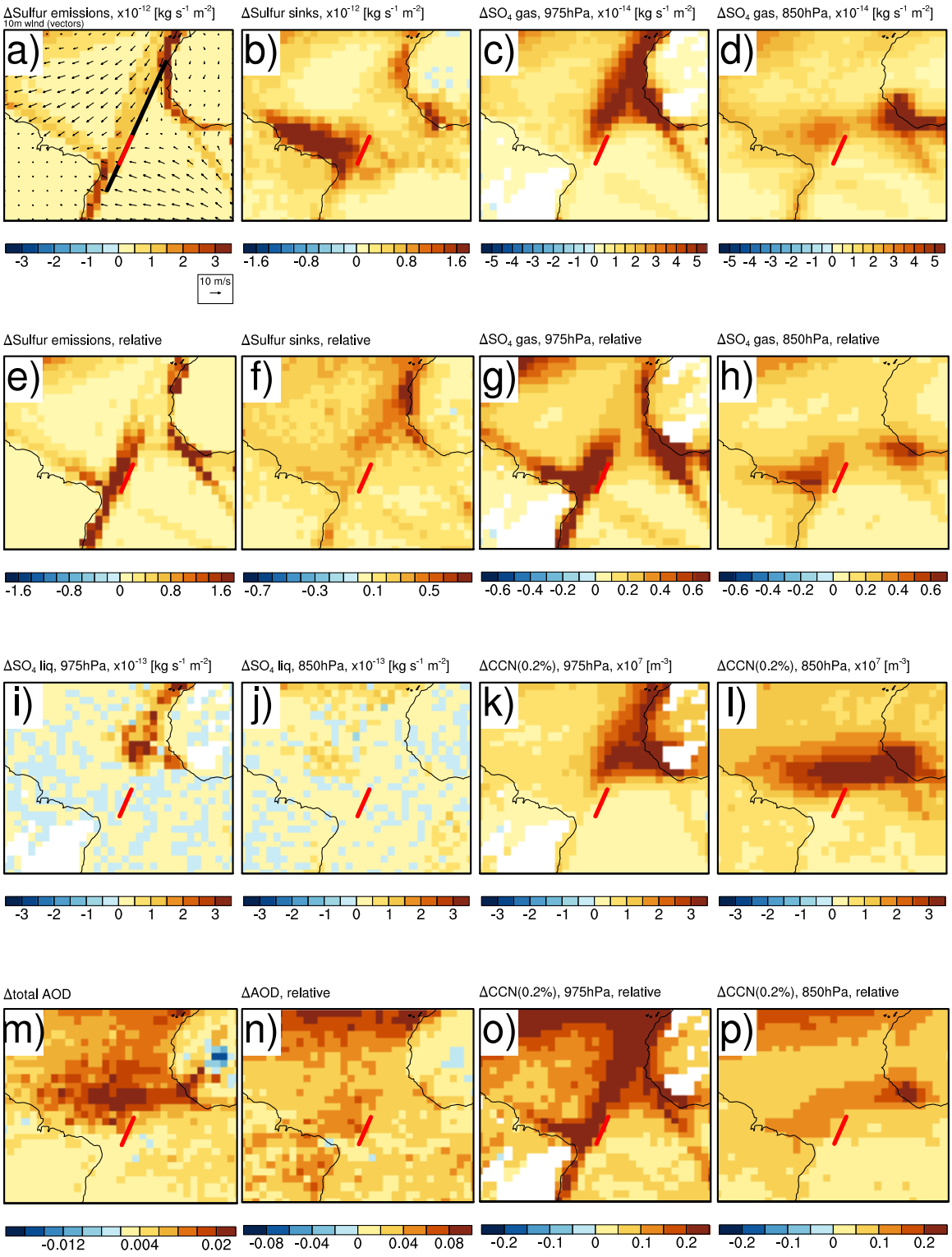

Figure S9: Ship-emission (simulation *Bsc*) induced MAM-mean absolute and relative changes of sulfur emissions and sinks (a, e and b, f, respectively), sulfate production from gas phase chemistry at 975 and 850 hPa (c, g and d, h, respectively), sulfate production from liquid phase chemistry (aqueous oxidation) at 975 and 850 hPa (i and j, absolute changes only), total AOD (m, n), CCN concentrations at 0.2% supersaturation at 975 and 850 hPa (k,o and l, p, respectively). Relative changes are derived after $\left(\frac{Bsc-CTRL}{CTRL}\right)$. Vectors in a) indicate the MAM-mean 10m wind direction and speed.

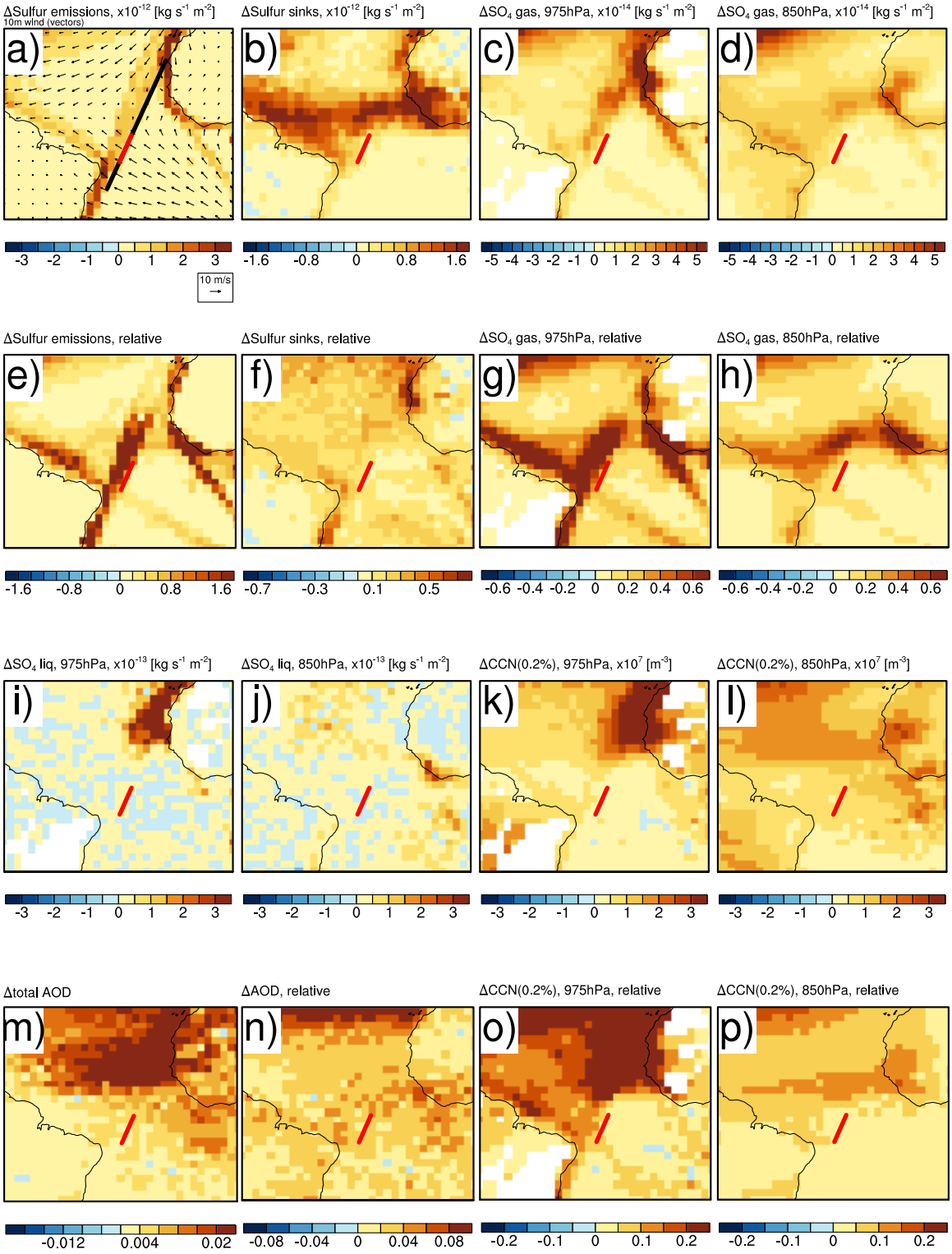

Figure S10: Same as Fig. S9, but for season JJA.

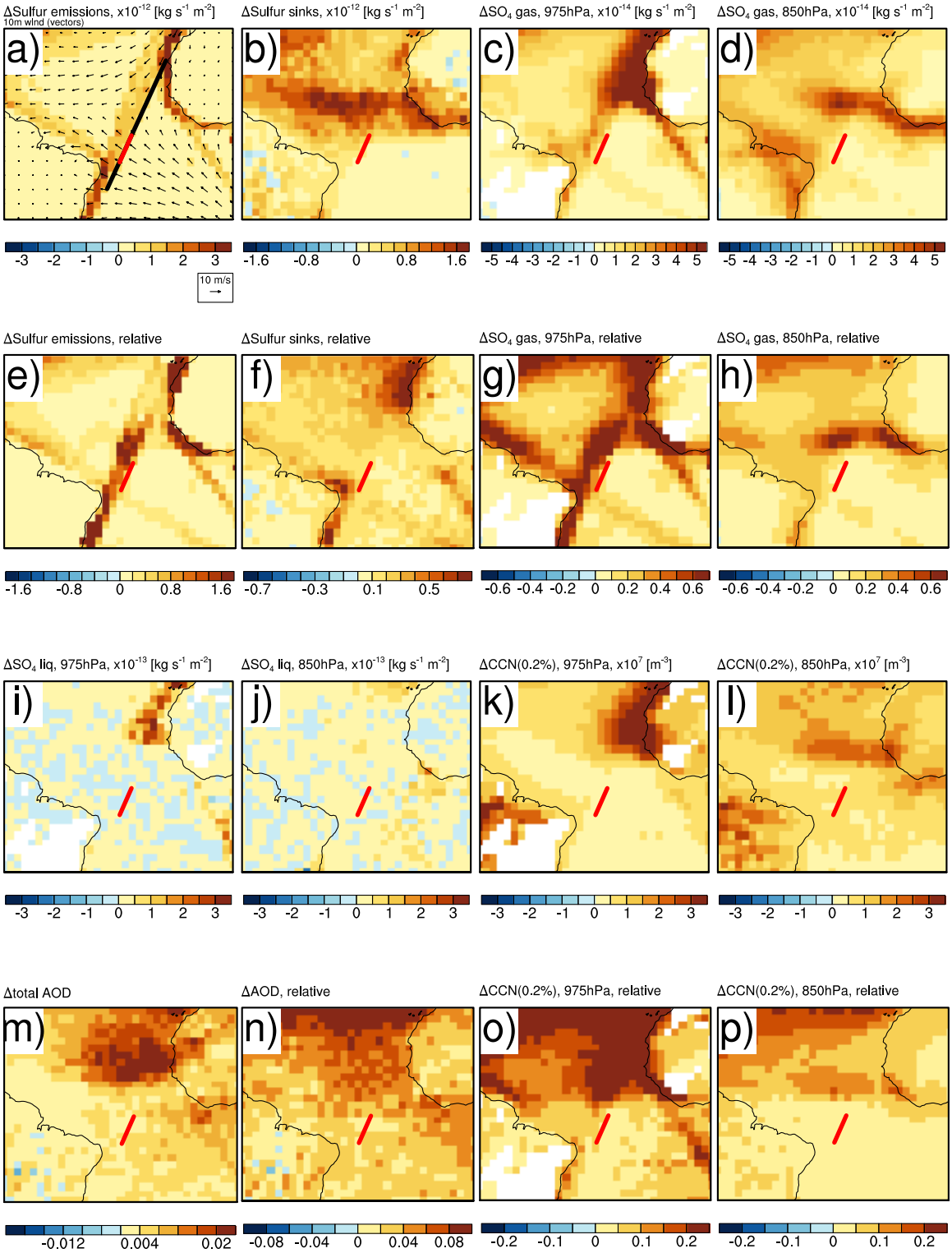

Figure S11: Same as Fig. S9, but for season SON.

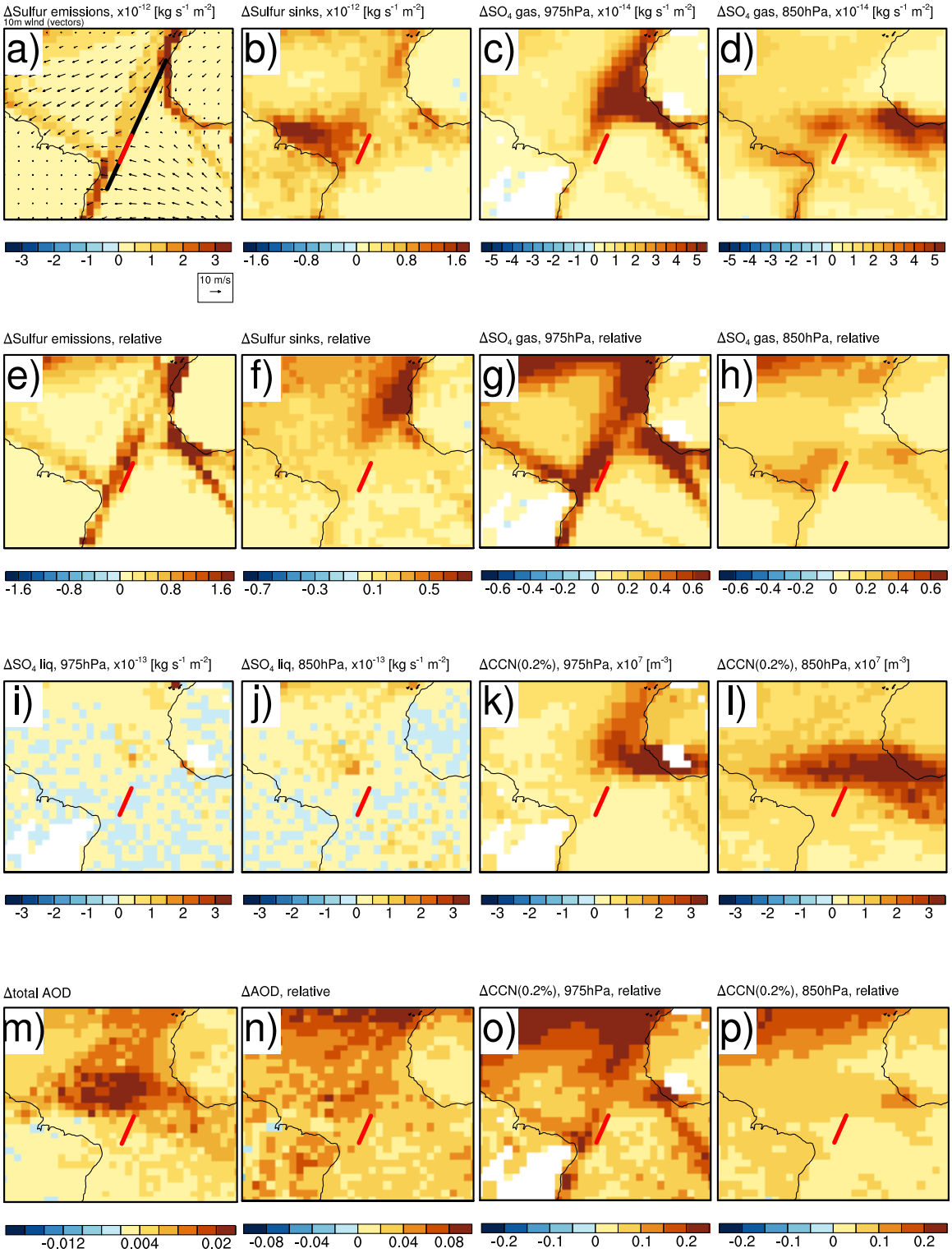

Figure S12: Same as Fig. S9, but for season DJF.

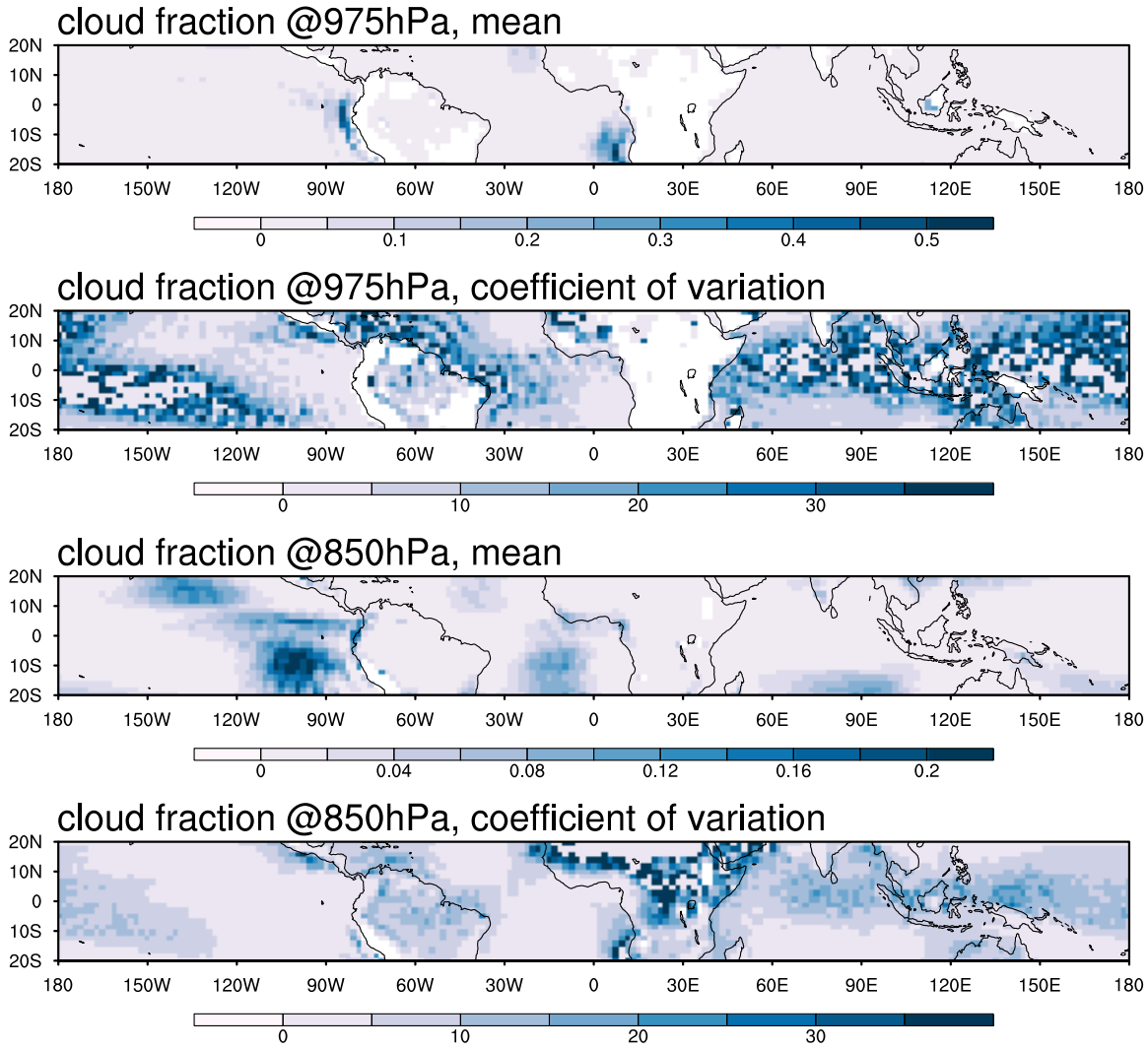

Figure S13: Five-year mean cloud fractions and the respective coefficients of variation at 975 and 850 hPa. The coefficient of variation is defined as the standard deviation divided by the mean value. Please note the different color scales for the first and third panel from the top.

5 Mean cloud fractions and cloud fraction variability at 975 and 850 hPa as simulated by ECHAM5-HAM

See Figure S13.

References

K. Peters, J. Quaas, and H. Graßl. A search for large-scale effects of ship emissions on clouds and radiation in satellite data. *J. Geophys. Res.-Atmos.*, 116:D24205, 2011. doi: 10.1029/2011JD016531.

K. Peters, P. Stier, J. Quaas, and H. Graßl. Aerosol indirect effects from shipping emissions:

sensitivity studies with the global aerosol-climate model ECHAM-HAM. *Atmos. Chem. Phys.*, 12(13):5985–6007, 2012. doi: 10.5194/acp-12-5985-2012.